Ensemble-Based Modelling of the NMR Spectra of Solid Solutions: Cation Disorder in $Y_2(Sn,Ti)_2O_7$

Robert F. Moran,[1] David McKay,[1] Paulynne C. Tornstrom,[2] Alex Aziz,[2] Arantxa Fernandes,[1] Ricardo Grau-Crespo[2]* and Sharon E. Ashbrook[1]*

[1]*School of Chemistry, EaStCHEM and Centre of Magnetic Resonance, University of St Andrews, St Andrews KY16 9ST, UK*

[2] *Department of Chemistry, University of Reading, Whiteknights RG6 6AD, UK*

Supporting Information

S1. Further information on DFT calculations

CASTEP[1-2] (version 8.0) DFT calculations were carried out using the PBE[3] exchange correlation functional and core-valence interactions were described by ultrasoft pseudopotentials,[4] accounting for scalar relativistic effects using ZORA. A planewave energy cutoff of 60 Ry (~816 eV) was used. The first Brillouin zone was sampled through a Monkhorst-Pack grid[6] with a k-point spacing of 0.04 2π Å^{-1}.

Geometry optimisation

Initially, geometry optimisations were carried out using the default values of `geom_energy_tol` and `elec_energy_tol` (*i.e.*, 5×10^{-5} eV /atom and 7×10^{-5} eV /atom). However, if an optimisation was repeated, small changes in the optimised geometry often led to surprisingly significant discrepancies in the subsequently calculated NMR parameters. To probe the repeatability of the geometry optimisation, a single pyrochlore unit cell of containing 12 Sn and 4 Ti on the 16 B sites (*i.e.*, $Y_2(Sn_{0.75}Ti_{0.25})_2O_7$) was used, with the distribution of the B site cations randomly generated. The geometry of this initial model was optimised from the same starting point twice, and the root-mean-square deviation (RMSD) between the two structures calculated, while the values of `geom_energy_tol` and `elec_energy_tol` used systematically decreased. A summary of the RMSD values is given in Table S1.1 and Figure S1.1. As `elec_energy_tol` is reduced, the RMSD steadily decreases. In contrast, there is only small fluctuation in the RMSD as `geom_energy_tol` is decreased. This suggests that the magnitude of `elec_energy_tol` is important for the repeatability of the geometry optimisations.

Table S1.1. RMSD between two identical structural models of $Y_2(Sn_{0.75}Ti_{0.25})_2O_7$, optimised from the same starting point using the same parameters, for varying values of `geom_energy_tol` and `elec_energy_tol`. When `geom_energy_tol` was varied `elec_energy_tol` was fixed at 1×10^{-5} eV / atom, whilst `geom_energy_tol` was fixed at 1×10^{-4} eV / atom when `elec_energy_tol` was varied.

`Geom_energy_tol` / eV / atom	RMSD / Å	`Elec_energy_tol` / eV / atom	RMSD / Å
1×10^{-4}	1.50×10^{-2}	1×10^{-5}	9.19×10^{-3}
1×10^{-5}	2.32×10^{-3}	1×10^{-6}	3.06×10^{-3}
1×10^{-6}	1.99×10^{-2}	1×10^{-7}	7.27×10^{-5}
1×10^{-7}	7.72×10^{-2}	1×10^{-8}	5.03×10^{-5}
		1×10^{-9}	1.07×10^{-5}

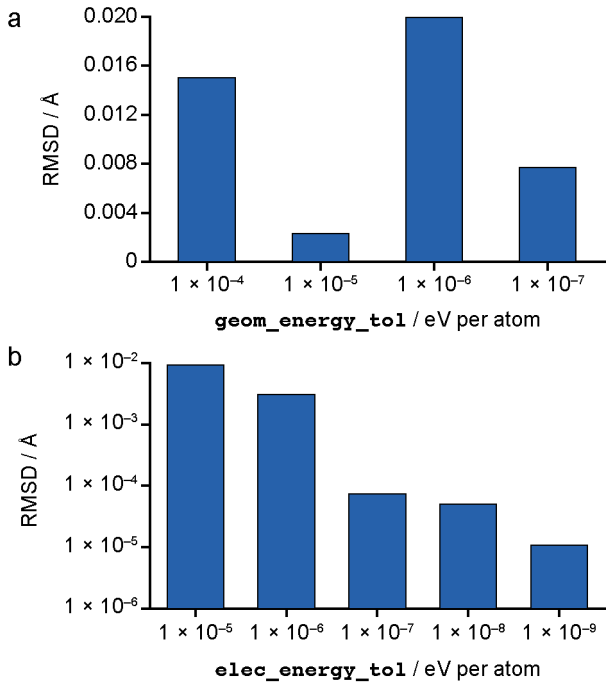

Figure S1.1. Bar charts showing the RMSD between two structural models of $Y_2(Sn_{0.75}Ti_{0.25})_2O_7$, optimised from the same starting point using the same parameters, plotted as a function of (a) `geom_energy_tol` and (b) `elec_energy_tol`.

Additionally, two separate sets of calculations were performed for an initial structural model of $Y_2(Sn_{0.5}Ti_{0.5})_2O_7$ (*i.e.*, with 8 Sn and 8 Ti atoms on the 16 B sites). In the first set of

calculations, an identical structural model was geometry optimised 20 separate times, using exactly the same parameters with an `elec_energy_tol` value of 1×10^{-5} eV per atom. In the second set an `elec_energy_tol` value of 1×10^{-9} eV per atom was used. Subsequently, $^{89}Y\ \delta_{iso}^{calc}$ were calculated (converted from σ_{iso}^{calc} as described below), and are shown in Figure S1.2. As shown in Figure S1.2a, there is a surprisingly significant variation in the $^{89}Y\ \delta_{iso}^{calc}$ calculated for the 20 optimised models when `elec_energy_tol` = 1×10^{-5} eV per atom, as shown by the differences between the blue points and the red points (the 16 $^{89}Y\ \delta_{iso}^{calc}$ for one selected model). In contrast, when `elec_energy_tol` = 1×10^{-9} eV per atom identical values of $^{89}Y\ \delta_{iso}^{calc}$ are observed for all 20 models (see Figure S1.2b)

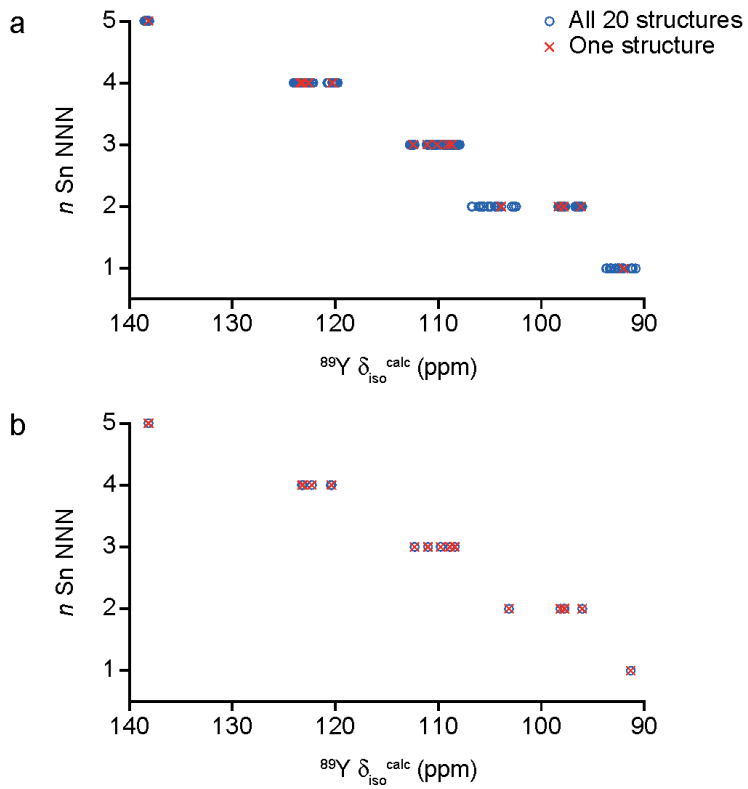

Figure S1.2. Plots of $^{89}Y\ \delta_{iso}^{calc}$ as a function of *n* Sn NNN for a set of 20 identical structural models of Y_2SnTiO_7 geometry optimised using `elec_energy_tol` of (a) 1×10^{-5} and (b) 1×10^{-9} eV per atom.

As a result of the above observations, an `elec_energy_tol` value of 1×10^{-9} eV per atom and a `geom_energy_tol` value of 1×10^{-5} eV per atom were used in all calculations reported in the main text.

Referencing and scaling

Calculations generate the absolute shielding tensor ($\boldsymbol{\sigma}^{calc}$) in the crystal frame, and diagonalization of the symmetric part yields the three principal components σ_{11}^{calc}, σ_{22}^{calc} and σ_{33}^{calc}. From these, $\sigma_{iso}^{calc} = (\sigma_{11}^{calc} + \sigma_{22}^{calc} + \sigma_{33}^{calc})/3$, the magnitude of the anisotropy or span, $\Omega^{calc} = \sigma_{11}^{calc} - \sigma_{33}^{calc}$ and the skew, $\kappa^{calc} = 3\,(\sigma_{22}^{calc} - \sigma_{iso}^{calc})/\Omega^{calc}$. To facilitate comparison to experiment σ_{iso}^{calc} values were converted to δ_{iso}^{calc}. For ^{89}Y, this was achieved by comparing experimental and calculated NMR parameters for the two end members, $Y_2Sn_2O_7$ and $Y_2Ti_2O_7$.[7] These are given in Table S1.2 and plotted in Figure S1.3. From the line of best fit in Figure S1.3a it can be seen that

$$\delta_{iso}^{calc} = -0.6258\,\sigma_{iso}^{calc} + 1736.7942\ . \qquad \text{(S1.1)}$$

In order to ensure easier comparison to experiment for Ω, the value of Ω^{calc} was also scaled (as used previously in Ref. 8), with

$$\Omega^{calc,sc} = 0.8070\,\Omega^{calc} + 78.52\ . \qquad \text{(S1.2)}$$

Table S1.2. Experimental and calculated ^{89}Y NMR parameters for $Y_2Sn_2O_7$ and $Y_2Ti_2O_7$.

	Calculated		Experimental	
	σ_{iso}^{calc} (ppm)	Ω^{calc} (ppm)	δ_{iso}^{exp} (ppm)	Ω^{exp} (ppm)
$Y_2Sn_2O_7$	2535.57	160.47	150[S7]	208[S8]
$Y_2Ti_2O_7$	2671.40	640.05	65[S7]	595[S8]

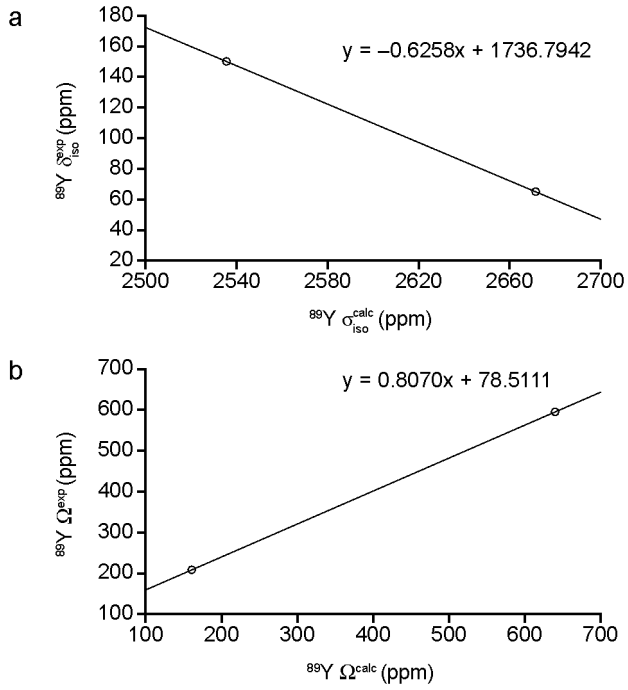

Figure S1.3. Plots of ^{89}Y experimental (a) δ_{iso} and (b) Ω against calculated (a) σ_{iso} and (b) Ω for $Y_2Sn_2O_7$ and $Y_2Ti_2O_7$.

For ^{119}Sn, the reference shielding was determined by comparing the experimental shift ($\delta_{iso}^{exp} = -582$ ppm[9]) and calculated shielding ($\sigma_{iso}^{calc} = 3184.49$ ppm) for $Y_2Sn_2O_7$. Using

$$\sigma_{ref} = \sigma_{iso}^{calc} + \delta_{iso}^{exp} \ , \qquad \text{(S1.3)}$$

gives $\sigma_{ref} = 2602.49$ ppm, and δ_{iso}^{calc} is then given by

$$\delta_{iso}^{calc} = \sigma_{iso}^{calc} - \sigma_{ref} \ . \qquad \text{(S1.4)}$$

Figure S1.4 shows the local atomic environments around the pyrochlore A site (occupied here by Y) and B site (occupied by either Sn or Ti), and the numbering scheme used to denote the different arrangements of the atoms on the six next nearest neighbour (NNN) B sites in each case.

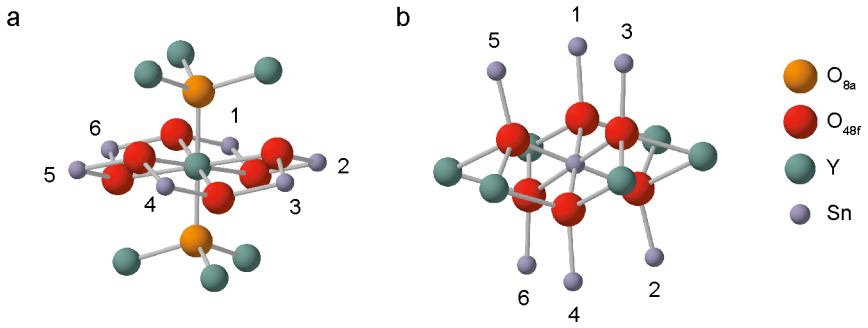

Figure S1.4. The local environment around (a) Y (A site) and (b) Sn (B site) in a $Y_2Sn_2O_7$ pyrochlore, showing the position of the six B site NNN, and the numbering scheme used.

S2. Calculation of thermodynamic properties

From the compete set of unique configurations generated by the Site Occupancy Disorder (SOD) program,[10] it is possible to derive thermodynamic parameters using statistical mechanics. The extent of occurrence of one particular configuration in the disordered solid, assuming configurational equilibrium, is described by a Boltzmann-like probability, which is calculated from the energy, E_m, of the configuration, and its degeneracy, g_m, (*i.e.*, the number of times that the configuration is repeated in the complete configurational space). This is given by

$$P_m = \frac{g_m}{Z} \exp\left(-E_m / RT\right) , \tag{S2.1}$$

where $m = 1, \ldots M$ (and M is the number of inequivalent configurations), R is the molar gas constant and Z is the partition function, which gives access to configurational free energies and entropies. In this way, it is possible to obtain temperature-dependent configurational thermodynamic functions and the equilibrium degree of disorder.[11] In this work, we consider the full disorder limit, formally $T \to \infty$, where the probability in Eqn. S2.1 reduces to

$$P_m = \frac{g_m}{\sum_m g_m} . \tag{S2.2}$$

In particular, the thermodynamics of mixing is investigated using the sub-regular solid solution model,[12] where the enthalpies are obtained in the full disorder limit as

$$H = \frac{\sum_m g_m H_m}{\sum_m g_m} , \tag{S2.3}$$

while the entropy at concentration x is given by the temperature-independent "ideal" expression

$$S_{\text{ideal}}(x) = -R[x \ln x + (1 - x) \ln (1 - x)] , \tag{S2.4}$$

and the enthalpy of mixing

$$\Delta H_{\mathrm{mix}} = H_x - (x\, H_{x=0} + (1-x)\, H_{x=1}) \ , \qquad \text{(S2.5)}$$

is fitted to an asymmetric polynomial, as explained in the main text. The free energy of mixing can then be obtained as

$$\Delta G_{\mathrm{mix}} = \Delta H_{\mathrm{mix}} - T\, S_{\mathrm{ideal}} \ , \qquad \text{(S2.6)}$$

which can be used to determine the stability of the solid solution with respect to phase separation. In all plots (here and in the main text) these quantities are quoted in units of kJ mol^{-1} per substitutable site. Within this model, the enthalpy of mixing is the only contribution to the excess free energy (defined as the difference between the free energy of mixing and the ideal term $-T\, S_{\mathrm{ideal}}$). Vibrational and pressure-volume contributions to the mixing thermodynamics are ignored, as they are typically small.

Figure S2.1 shows a plot of calculated enthalpy of mixing (ΔH_{mix}) for the individual atomic configurations generated by SOD, as a function of the composition. A similar plot showing the average of the configuration energies weighted only by their corresponding degeneracies (*i.e.*, the limit of full disorder) is shown in Figure 1a of the main text.

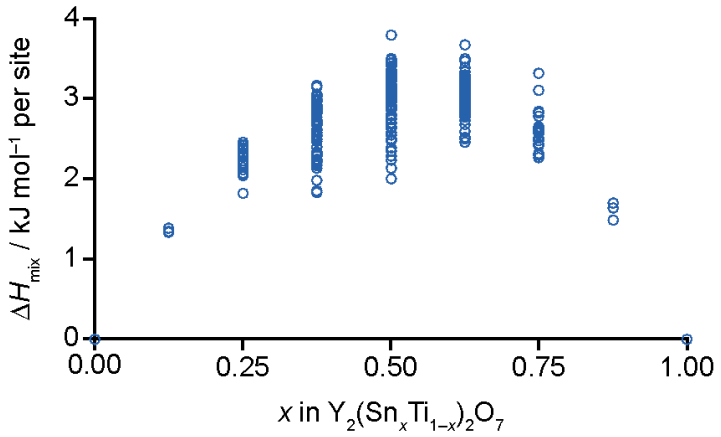

Figure S2.1. Plot of calculated enthalpy (ΔH_{mix}) of mixing for the individual atomic configurations of $Y_2(Sn_xTi_{1-x})_2O_7$ generated by SOD, as a function of the composition.

S3. Decomposition of spectral contributions

Figure S3.1 shows ^{89}Y and ^{119}Sn MAS NMR spectra for $Y_2(Sn_xTi_{1-x})_2O_7$, simulated as described in the main text by summing the spectra for each SOD-generated structural model, weighted by the corresponding configurational degeneracy, and decomposed according to the contributions from species with different NNN arrangements.

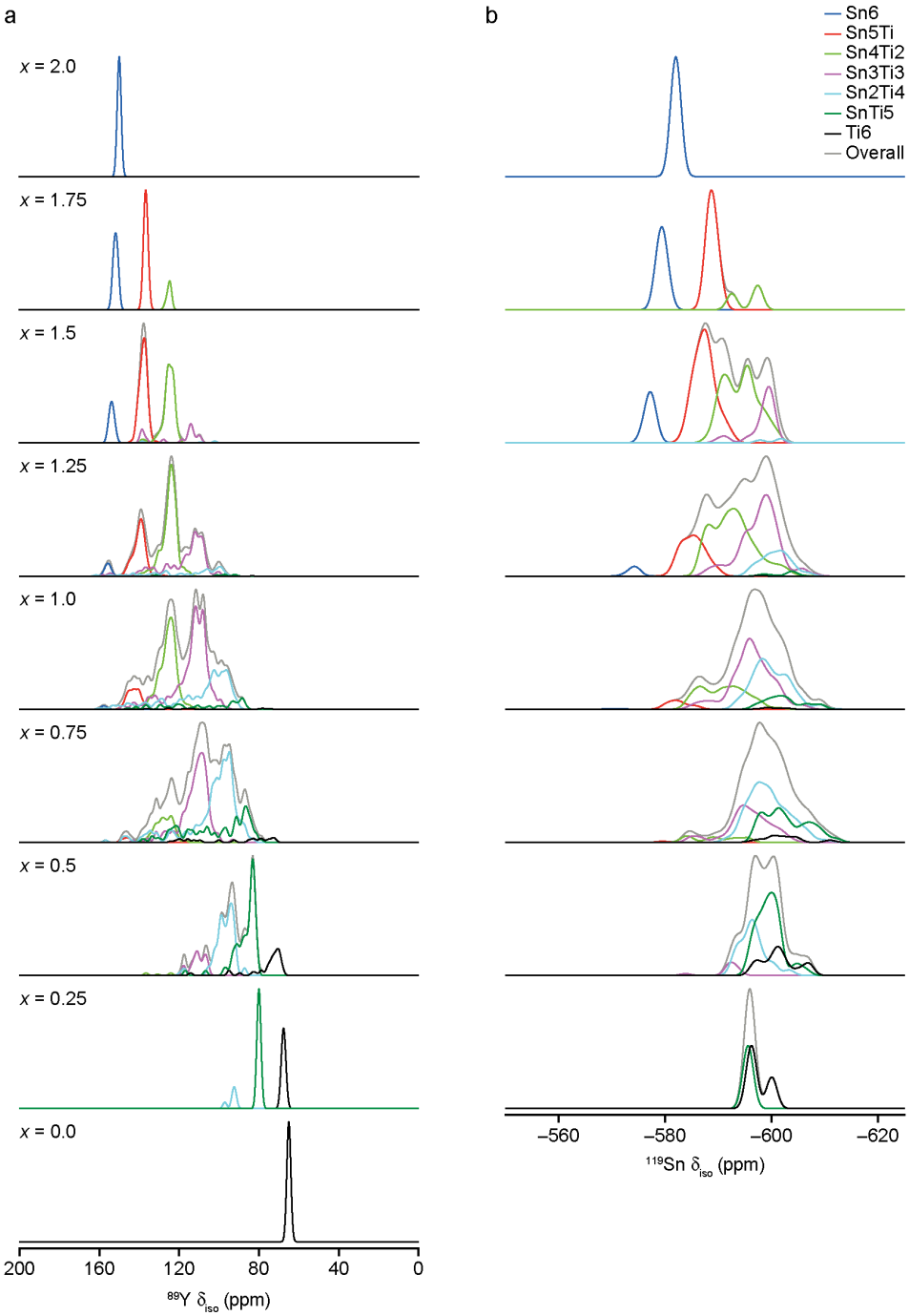

Figure S3.1. Simulated (a) ^{89}Y and (b) ^{119}Sn MAS NMR spectra for $Y_2(Sn_xTi_{1-x})_2O_7$ in the limit of full disorder, decomposed according to *n* Sn NNN.

S4. Cluster-like models of disorder in $Y_2(Sn,Ti)_2O_7$

Figure S4.1 plots ^{89}Y and ^{119}Sn $\delta_{iso}{}^{calc}$ against *n* Sn NNN for a series of calculations where the environment of one Y (or Sn) species in $Y_2Sn_2O_7$ or $Y_2Ti_2O_7$ was systematically modified to include the 13 possible NNN arrangements shown in Figure 1a of the main text (see Figure S1.4 for the numbering scheme). These calculations are, in principle, the same as those shown in previous work,[13-14] but have been carried out using the parameters described in the Computational Methods section of the main text (*i.e.*, with the version of the code, pseudopotentials, relativistic corrections and convergence criteria used in this work).

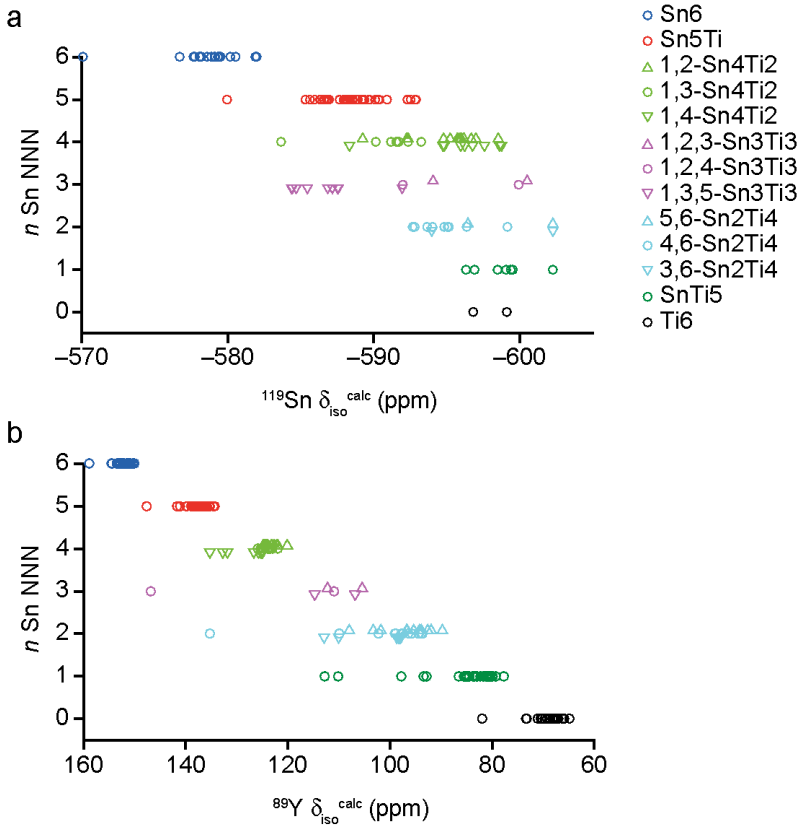

Figure S4.1. Plots of (a) ^{89}Y and (b) ^{119}Sn $\delta_{iso}{}^{calc}$ as a function of the number of Sn NNN, *n*, for all species in cluster-based structural models where the 6 NNN cations are modified, as shown in Figure 1a of the main text.

S5. ^{89}Y anisotropic shielding

Figure S5.1a shows a plot of ^{89}Y Ω^{calc} against the number, *n*, of Sn NNN, for all Y species within SOD-generated structural models of $Y_2(Sn,Ti)_2O_7$, showing a systematic decrease in the average value of Ω^{calc} of ~80 ppm per Sn NNN substituted, in good agreement with previous work using cluster-based models.[15] Figure S5.1b reveals the dependence of ^{89}Y Ω^{calc} on the mean Y-O_{8a} bond distance.

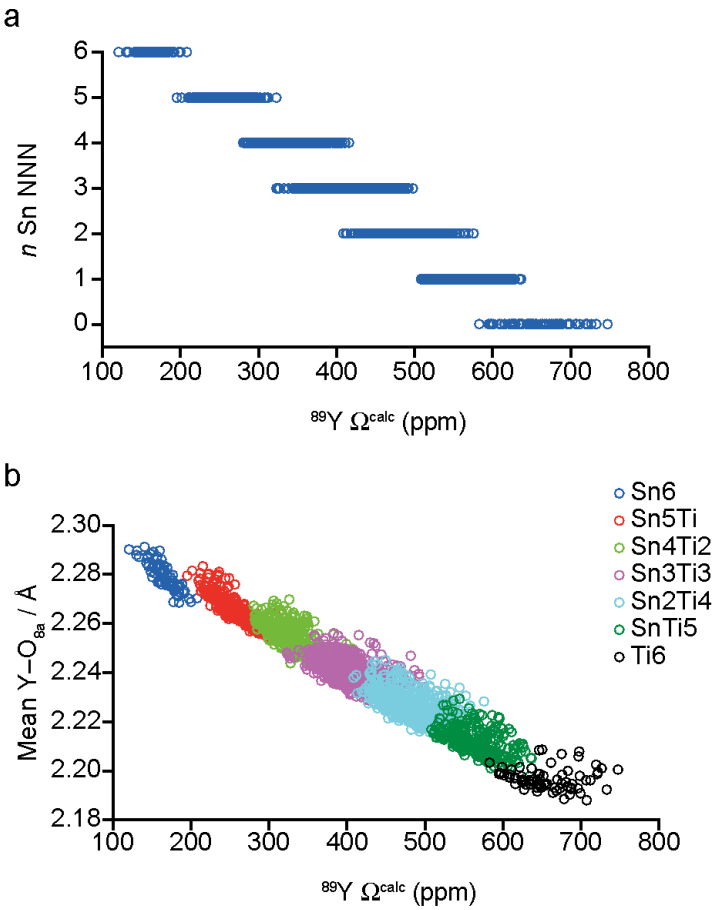

Figure S5.1. Plots of ^{89}Y Ω^{calc} as a function of (a) the number of Sn NNN, *n*, and (b) mean Y-O_{8a} bond distance, for all SOD-generated structural models of $Y_2(Sn,Ti)_2O_7$.

S6. Simulated sub spectra for structural models

File S6.1 shows a movie containing the simulated ^{89}Y MAS NMR sub spectra for each structural model of Y_2SnTiO_7 (shown normalised, *i.e.*, not accounting for any configurational degeneracy) in order of increasing energy. It is clear these are very different to each other, and each is very different to the experimental spectrum. The movie in File S6.2 shows the summation of the same sub spectra in order of increasing energy. In this movie, spectra are weighted only by the configurational degeneracy of the corresponding structural model (*i.e.*, not by any additional Boltzmann weighting). It is clear that good agreement with the experimental spectra is obtained only after the vast majority of structural models are combined.

Figure S6.1 shows the ^{89}Y MAS NMR spectrum simulated for structural model 56 (ΔH_{mix} = 3.07 kJ mol^{-1} per substituted atom, g_m = 192) of Y_2SnTiO_7, the model closest to the special quasi-random structure (SQS[16]). Although the simulated spectrum has better agreement with experiment than those for many of the other individual structural models (see File S6.1), it isn't possible to reproduce the summed predicted spectrum or the experimental NMR spectrum with a single "average" structure, owing the sensitivity of the NMR parameters to the specific local environment.

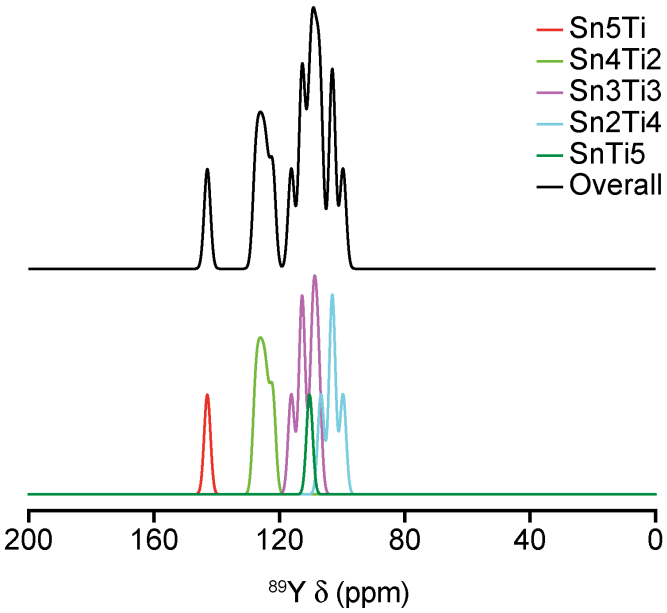

Figure S6.1. Simulated ^{89}Y MAS NMR spectrum for structural model 56 of Y_2SnTiO_7, also shown decomposed into the contributions arising from Y species with different numbers of Sn NNN.

S7. Relative energies of mixing on substitution

Figure 2 in the main text and Figure S2.1 reveal that the plots of the energies of mixing are slightly asymmetric with respect to composition, *i.e.*, it is relatively slightly easier to substitute the larger Sn^{4+} cation into a Ti-rich pyrochlore than *vice versa*. For example, for the three distinct structural models of $Y_{16}Sn_{14}Ti_2O_{48}$ (*i.e.*, $x = 0.875$) $\Delta H_{mix} = 0.28$, 0.27 and 0.25 eV, while for $Y_{16}Sn_2Ti_{14}O_{48}$ (*i.e.*, $x = 0.125$) $\Delta H_{mix} = 0.22$, 0.22 and 0.23 eV. Although this is perhaps a surprising observation, it appears to result from the increased covalency of the Sn-O bond, rather than simply the size difference between Sn and Ti.

Figure 5 in the main text shows that B-site substitution can lead to significant distortions in the structure (and correspondingly large changes in $^{89}Y\ \delta_{iso}^{calc}$). This results in a movement of Y away from the centrepoint defined by the six surrounding B site cations, leading to a deviation of the O_{8a}-Y-O_{8a} bond angle away from the value of 180° observed for the ideal pyrochlore structure. Depending upon the arrangement of Sn and Ti on the surrounding B sites, this can also result in a distribution of Sn-O_{48f} and/or Ti-O_{48f} bond distances (and in the Y-O_{48f} bond distances). It is clear from Figure 5, however, that these distortions are more significant for Ti-rich systems. When Sn^{4+} is substituted into a Ti-rich structure, the more ionic nature of the Ti-O bonds is able to accommodate the larger cation, with subsequent distortions away from the ideal geometry then able to reduce the energy of the system. In contrast, the more covalent nature of Sn-O bonding gives less structural flexibility upon the substitution of the smaller Ti^{4+} into a Sn-rich pyrochlore. This is shown in Figure S7.1, where for $x = 0.125$ (*i.e.*, $Y_{16}Sn_2Ti_{14}O_{48}$), a large distribution of Ti-O_{48f} distances is seen as the structure distorts to accommodate the larger Sn^{4+} cation (Figure S7.2c). In contrast, a smaller range of Sn-O_{48f} distances is seen in Figure S7.2b for $x = 0.875$ (*i.e.*, $Y_{16}Sn_{14}Ti_2O_{48}$), confirming the less flexible nature of the stannate-rich pyrochlore. Figure S7.1a also shows a large range of Ti-O_{48f} bond lengths when Ti^{4+} is substituted into the stannate pyrochlore, confirming that, despite $Y_2Ti_2O_7$ pyrochlore itself being stable, Ti^{4+} is not able to satisfy the bonding requirements of the surrounding oxygens in such a

heavily Sn-rich material, owing to the more covalent nature of the Sn-O bond, leading to the higher energies of mixing observed.

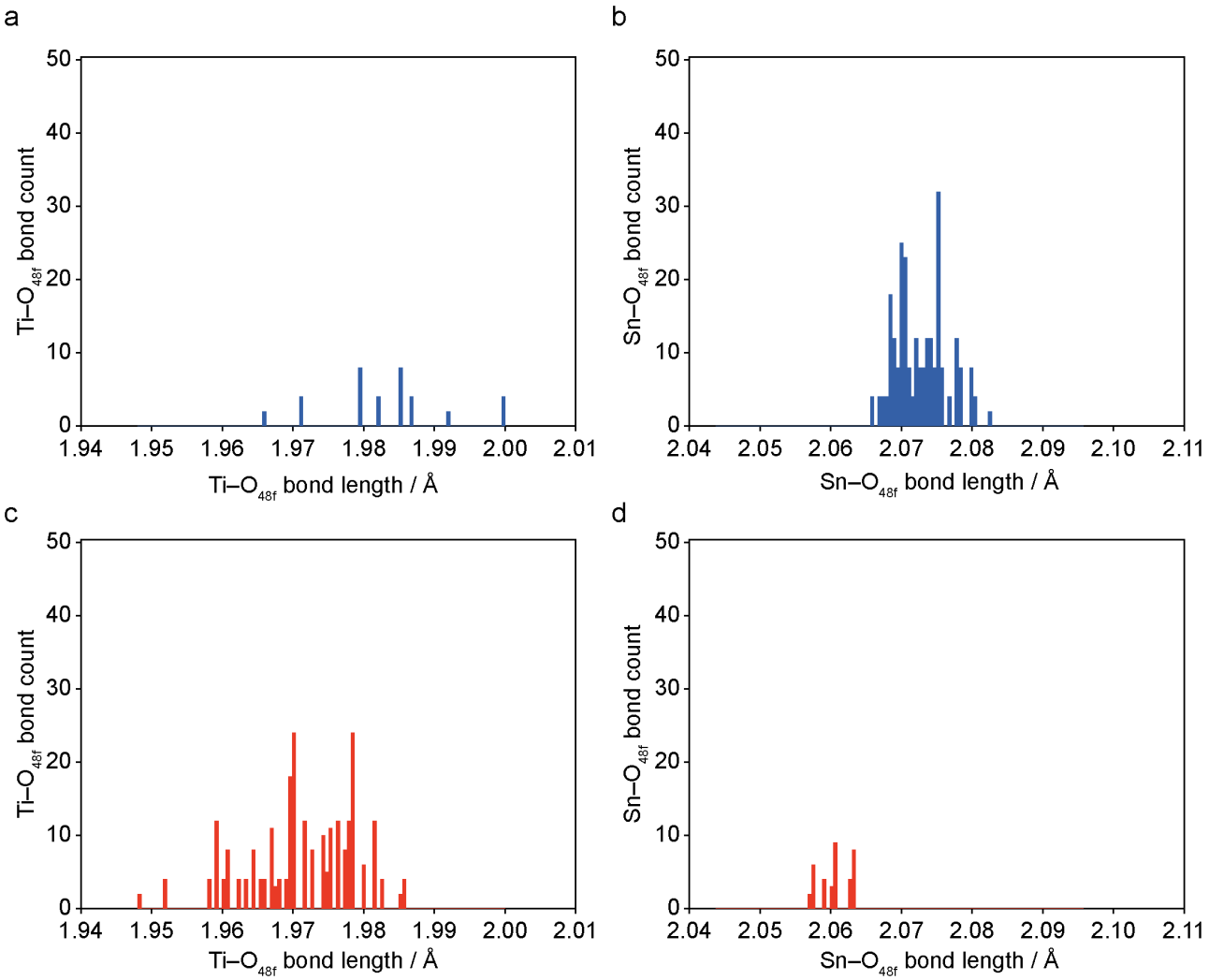

Figure S7.1 Histogram showing the range of (a, c) Ti-O_{48f} and (b, d) Sn-O_{48f} bond lengths for (a, b) $x = 0.875$ ($Y_{16}Sn_{14}Ti_2O_{48}$) and (c, d) $x = 0.125$ ($Y_{16}Sn_2Ti_{14}O_{48}$).

Figure S7.2 plots the mixing enthalpy of the lowest energy structural model for each composition of $Y_2(Sn_xTi_{1-x})_2O_7$ against the mean deviation of the O_{8a}–Y–O_{8a} bond angle away from 180°. This shows that as the composition varies from $x = 0$ ($Y_2Ti_2O_7$) to $x = 0.5$ (Y_2SnTiO_7), the energies are relatively low and the distortion is relatively large. However, on further variation from $x = 0.5$ to 1, the distortion decreases rapidly, but the energy increases, remaining high for 0.625 and 0.75 (which are both higher than for $x = 0.5$).

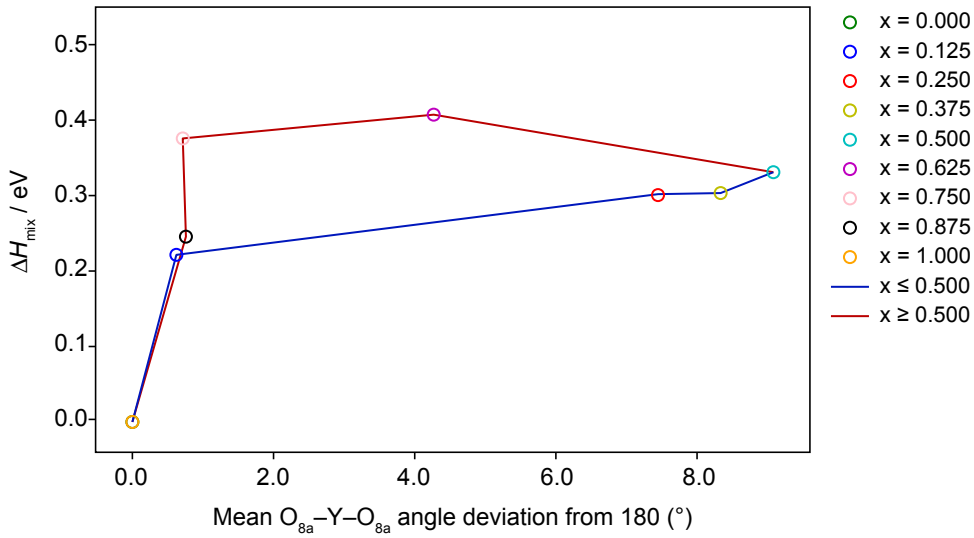

Figure S7.2 Plot of the enthalpy of mixing against the mean deviation of the O_{8a}–Y–O_{8a} bond angle for the most stable structural model for each composition of $Y_2(Sn_xTi_{1-x})_2O_7$.

S8. References

1. Pickard, C. J.; Mauri, F. All-Electron Magnetic Response with Pseudopotentials: NMR Chemical Shifts. *Phys. Rev. B: Condens. Matter Matter. Phys.*, **2001**, *63*, 245101.

2. Clark, S. J.; Segall, M. D.; Pickard, C. J.; Hasnip, P. J.; Probert, M. J.; Refson, K.; Payne, M. C. First-Principles Methods using CASTEP. *Z. Kristallogr.* **2005**, *220*, 567-570.

3. Perdew, J. P.; Burke, K.; Ernzerhof, M. Generalized Gradient Approximation Made Simple. *Phys. Rev. Lett.* **1996**, *77*, 1865-1868.

4. Vanderbilt, D. Soft Self-Consistent Pseudopotentials in a Generalized Eigenvalue Formalism. *Phys. Rev. B: Condens. Matter Mater. Phys.* **1990**, *41*, 7892-7895.

5. Yates, J. R.; Pickard, C. J.; Payne, M. C.; Mauri, F. Relativistic Nuclear Magnetic Resonance Chemical Shifts of Heavy Nuclei with Pseudopotentials and the Zeroth-Order Regular Approximation. *J. Chem. Phys.* **2003**, *118*, 5746-5743.

6. Monkhorst, H. J.; Pack, J. D. Special Points for Brillouin-Zone Integrations. *Phys. Rev. B* **1976**, *13*, 5188-5192.

7. Grey, C. P.; Smith, M. E.; Cheetham, A. K.; Dobson, C. M.; Dupree, R. Yttrium-89 Magic Angle Spinning NMR Study of Rare-Earth Pyrochlores: Paramagnetic Shifts in the Solid State. *J. Am. Chem. Soc.*, 1990, **112**, 4670-4675.

8. Mitchell, M. R.; Carnevale, D.; Orr, R.; Whittle, K. R.; Ashbrook S. E. Exploiting the Chemical Shielding Anisotropy to Probe Structure and Disorder in Ceramics: ^{89}Y MAS NMR and First-Principles Calculations. *J. Phys. Chem. C* **2012**, *116*, 4273-4286.

9. Grey, C. P.; Dobson, C. M.; Cheetham, A. K.; Jakeman, R. J. B. Studies of Rare-Earth Stannates by ^{119}Sn MAS NMR. The Use of Paramagnetic Shift Probes in the Solid State. *J. Am. Chem. Soc.* **1989**, *111*, 505-511.

10. Grau-Crespo, R.; Hamad, S.; Catlow C. R. A.; de Leeuw, N. H. Symmetry-Adapted Configurational Modelling of Fractional Site Occupancy in Solids. *J. Phys.: Condens. Matter*, **2007** *19*, 256201.

11. Grau-Crespo, R.; Waghmare, U. V. *Simulation of Crystals with Chemical Disorder at Lattice Sites*, in *Molecular Modeling for the Design of Novel Performance Chemicals and Materials*, B. Rai, Ed.; CRC Press. 2012; p. 299-322.

12. Ganguly, J. *Thermodynamics in Earth and Planetary Sciences*. Springer-Verlag, 2008.

13. Reader, S. W.; Mitchell, M. R.; Johnston, K. E.; Pickard, C. J.; Whittle, K. R.; Ashbrook, S. E. Cation Disorder in Pyrochlore Ceramics: ^{89}Y MAS NMR and First-Principles Calculations. *J. Phys. Chem. C* **2009**, *113*, 18874-18883.

14. Mitchell. M. R.; Reader, S. W.; Johnston, K. E.; Pickard, C. J.; Whittle K. R., Ashbrook, S. E. ^{119}Sn MAS NMR and First-Principles Calculations for the Investigation of Disorder in Stannate Pyrochlores. *Phys. Chem. Chem. Phys.* **2011**, *13*, 488-497.

15. Mitchell, M. R.; Carnevale, D.; Orr, R.; Whittle K. R.; Ashbrook, S. E. Exploiting the Chemical Shielding Anisotropy to Probe Structure and Disorder in Ceramics: ^{89}Y MAS NMR and First-Principles Calculations. *J. Phys. Chem. C*, **2012**, *116*, 4273-4286.

16. Zunger, A.; Wei, S. H.; Ferreira, L. G.; Bernard, J. E. Special Quasirandom Structures. *Phys. Rev. Lett.* **1990**, *65*, 353-356.